Oxidation ruled transition from normal to anomalous periodic structures with femtosecond laser irradiation on Cr/Si films

HONGBO XIE,[1,2] BO ZHAO,[3] YUHAO LEI,[1] ZHI YU,[1] JINLUO CHENG,[1] AND JIANJUN YANG[1,*]

[1]*GPL Photonics Laboratory, State Key Laboratory of Applied Optics, Changchun Institute of Optics, Fine Mechanics and Physics, Chinese Academy of Sciences, Changchun 130033, China*
[2]*University of Chinese Academy of Sciences, Beijing 100049, China*
[3]*Department of Electronic Information and Physics, Changzhi University, Shanxi 046011, China*
[*]*jjyang@ciomp.ac.cn*

Abstract: Elucidation of the underlying physics for laser-induced periodic surface structures (LIPSSs) is of great importance for their controllable fabrication. We here demonstrate a periodic structure transition from normal to anomalous morphology, upon femtosecond laser irradiation on 50-nm thick Cr/Si films in an air pressure-tunable chamber. As the air pressure gradually decreases, the amount of surface oxide induced by preceding laser pulses is found to reduce, and eventually triggering the structure evolution from the anomalously oriented subwavelength to normally oriented deep-subwavelength LIPSSs. The intriguing structure transition is explained in terms of the competitive excitation between the transverse-electric scattered surface wave and transverse-magnetic hybrid plasmon wave, which is ruled by the thickness of the preformed oxide layer indeed.

1. Introduction

Femtosecond laser-induced periodic surface structures (LIPSSs) have attracted an increasing attention over the past few decades owing to their abundant physical phenomena and wide applications [1–7]. So far, previous studies have identified that two types of periodic structures can be produced on the metal surface upon irradiation of the linearly polarized femtosecond laser, with their spatial orientation either perpendicular or parallel to the laser polarization [8–18]. The former is the so-called normal LIPSSs (or n-LIPSSs) with a usually spatial period at the subwavelength ($\lambda/2 < \Lambda < \lambda$) level [8–13], and their formation mechanism is generally ascribed to the surface plasmon excitation [19,20]. The latter is often named as the anomalous LIPSSs (or a-LIPSSs), exhibiting a spatial period in subwavelength or deep-subwavelength ($\lambda/2 < \Lambda < \lambda$) scales [14–18], and their formation mechanism is usually explained by the scattering of surface roughness to the laser light [18,21].

Recently, some authors have declared that the above types of LIPSSs are closely dependent on the incident laser fluence (*i.e.* the strong laser fluence for n-LIPSSs and the weak laser fluence for a-LIPSSs) [14,16,17,22]. Moreover, Dostovalov *et al.* has demonstrated that these two types of structures are also determined by the laser scanning velocity (the lower scanning velocity for a-LIPSSs and the higher scanning velocity for n-LIPSSs) on the 28 nm thick Cr/glass material in air [23]. Besides, they concluded that the reason for structure transition is the reduction of periphery area and the preservation of central area in the irradiation spot with an increasing scanning velocity, where the periphery area with weak oxidation is preferable to generate a-LIPSSs; however, the central area with strong oxidation tends to form n-LIPSSs. In order to further clarify the role of oxidation on the formation of LIPSSs and their mutual

transitions, the implementation of laser processing experiments at different ambient air pressures is desirable.

In this paper, we report the influence of material oxidation on the transition of LIPSSs on 50-nm thick Cr/Si films under irradiation of femtosecond laser at different ambient air pressures. When the air pressure declines from $P = 10^5$ Pa down to 10^{-5} Pa, the laser-induced structures undergo an evolvement from the bulge profiled subwavelength a-LIPSSs into the ablative profiled deep-subwavelength n-LIPSSs. The Raman measurements and analyses reveal that such structure evolution is closely related to the thickness of the oxide layer induced by the preceding pulses, which consequently determines the excitation of two different surface waves.

2. Experimental section

A schematic diagram of the experimental setup is illustrated in Fig. 1, wherein a commercial Ti:sapphire regenerative amplifier laser system (Spectra Physics HP-Spitfire 50) is used to generate linearly polarized 40 fs pulses with a center wavelength of 800 nm at a repetition rate of 1 kHz. After passing through an attenuator consisting of a half-wave plate and a Glan prism, the femtosecond laser pulses are focused by a plano-convex lens (focal length $f = 300$ mm) into a pressure-tunable chamber (PT-Chamber), in which the residual air pressure can be continuously varied from $P = 1.0 \times 10^5$ Pa to 1.0×10^{-5} Pa via the coordination of a sophisticated mass flow meter and vacuum pump valves. In this chamber, a 50 nm thick Cr/Si material (prepared by evaporating the Cr film onto an \lt100\gt oriented single crystal silicon) is mounted onto a three-dimensional translation stage. The sample surface is positioned approximately 4 mm in front of the laser focal plane, generating a beam spot with a diameter of $\varphi = 141.4$ μm ($1/e^2$ intensity). During the experiments, the sample is scanned with a velocity of $V = 2$ μm/s, along the direction perpendicular to both the propagation and polarization of the laser beam, giving rise to nearly $N_{eff} = 7.07 \times 10^4$ pulses partially overlapped within one laser spot area. After the laser treatment, the surface morphology in the laser-irradiated areas is examined by a field emission scanning electron microscopy (SEM, HITACHI, S-4800), a laser confocal microscopy (Keyence, VK-X1000), and an atomic force microscopy (AFM, BRUKER, Multimode 8).
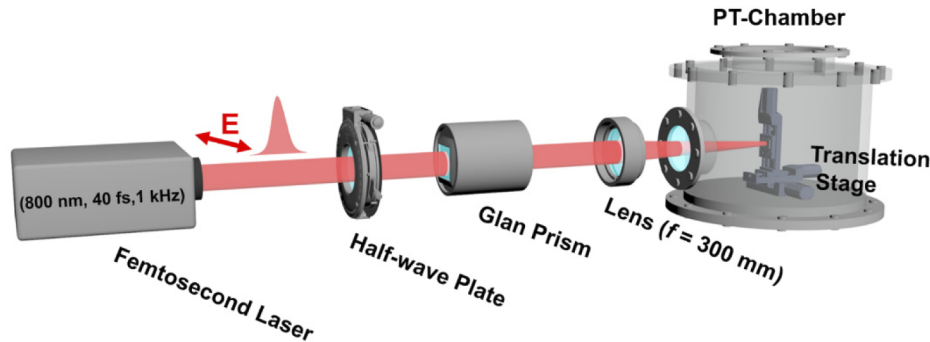

Fig. 1. Schematic diagram of the experimental setup for femtosecond laser structuring of 50-nm thick Cr/Si films at different air pressures. PT-Chamber indicates the pressure-tunable chamber. The red double-arrow represents the direction of the laser polarization.

3. Results and discussions

Through varying the residual air pressure inside the PT-Chamber, we investigated the oxidation effect on the generation of laser-induced surface structures. Figure 2 shows the structure formation on Cr/Si samples after irradiation by a fixed laser energy $E_0 = 4.21$ μJ at five different pressure levels. The SEM images are complemented with the corresponding two-dimension fast Fourier

transformation (2D-FFT) images, revealing the spatial frequency and orientation of the structures in the Fourier space. For the case of atmospheric pressure, one-dimensional (1D) periodic structures are observed on the sample surface, as shown in Fig. 2(a). The structures are featured with a period about $\Lambda = 701$ nm close to the laser wavelength and an anomalous orientation parallel to the laser polarization. These structures are similar to the observation in the previous reports [15,18] and can be categorized as the a-LIPSSs. The structural characterizations are also visualized by the spatial frequency spots with a horizontal alignment and an interval of 1.43 μm^{-1} in the 2D-FFT image. Whereas, as the air pressure is slightly decreased to $P = 2.0 \times 10^3$ Pa, the formation of a-LIPSSs becomes less pronounced. Meanwhile, a large number of nanoholes with a feature size of about 108 nm are regularly generated on the ridge areas [Fig. 2(b)]. The measured spatial periods of such nanohole arrays approximate $\Lambda = 753$ nm and 462 nm in the horizontal and vertical directions, respectively. Such structure variations can be also identified by the additional frequency components below and above the bright spots centrally distributed in the corresponding 2D-FFT image (see the yellow dotted box).
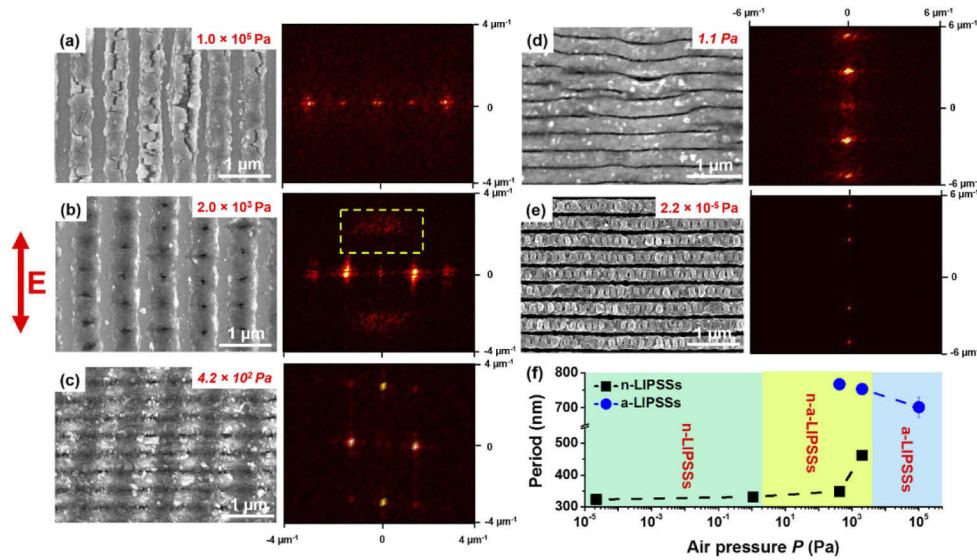
Fig. 2. Observed transition on the 50-nm thick Cr/Si film after irradiation of a laser energy $E_0 = 4.21$ µJ at different air pressures: (a) $P = 1.0 \times 10^5$ Pa; (b) $P = 2.0 \times 10^3$ Pa; (c) $P = 4.2 \times 10^2$ Pa; (d) $P = 1.1$ Pa; (e) $P = 2.2 \times 10^{-5}$ Pa. Left column represents the SEM images; right column for the corresponding 2D-FFT images. (f) Measured period variations for the laser-induced structures at different air pressures. The red double-arrow indicates the direction of laser polarization.

As the air pressure is further reduced to $P = 4.2 \times 10^2$ Pa, the laser-induced structures are found to change into 2D spatial distribution [Fig. 2(c)]. The formation of a-LIPSSs becomes much less pronounced, and the previous nanoholes seem to be spatially extended along the horizontal direction and then joined together forming new periodic nanogroove structures. In contrast to the aforementioned a-LIPSSs, the groove arrays are featured by a significantly reduced spatial period of $\Lambda = 349$ nm (in the deep-subwavelength scale) and an orientation perpendicular to the laser polarization, which can be categorized as the n-LIPSSs. In addition, the peculiar structure characterizations are also clarified in the 2D-FFT image with the rectangular distribution for the distinct frequency spots.

However, for the higher vacuum conditions ($P = 1.1$ Pa and 2.2×10^{-5} Pa), the laser-induced structures are found to transform into 1D spatial distribution again. Specifically, the subwavelength

a-LIPSSs completely disappear, and the laser-irradiated areas are only decorated with the deep-subwavelength n-LIPSSs, as shown in Figs. 2(d)-(e). Correspondingly, the discrete frequency spots in the Fourier space change into the vertical alignment. In contrast to the case of $P = 1.1$ Pa, the n-LIPSSs generated at $P = 2.2 \times 10^{-5}$ Pa present a more regular and clearer appearance without bending, breaking and bifurcation. In addition, anomalously oriented fine structures with the spatial period of 157 ± 9.5 nm can be also observed on the surface of n-LIPSSs at $P = 2.2 \times 10^{-5}$ Pa, which can be ascribed to the self-organization of molten materials flowing out of the nearby grooves due to Marangoni liquid instability [24]. Figure 2(f) plots the periodicity variations of laser-induced structures at different air pressures. It reveals that with reducing the air pressure, the period of a-LIPSSs tends to increase progressively from $\Lambda = 701.6$ nm to 766.9 nm, whereas the period of n-LIPSSs remains constant in the deep-subwavelength scale except for a small change at $P = 4.2 \times 10^2$ Pa. In general, an interesting structure transition is convincingly demonstrated on the Cr/Si sample via varying the residual air pressure in the PT-Chamber.

In addition, detailed morphology analyses for the laser-induced structures are also provided. Figures 3(a)-(b) show the typical AFM images for the a-LIPSSs produced at $P = 1.0 \times 10^5$ Pa and 2.0×10^3 Pa, respectively. It is found that these structures present bulging-like profiles above the initial surface of Cr film. The average modulation height of a-LIPSSs decreases from 120 nm to 52.6 nm with the decline of air pressure from $P = 1.0 \times 10^5$ Pa to $P = 2.0 \times 10^3$ Pa. Moreover, the average modulation depth for the nanoholes formed at $P = 2.0 \times 10^3$ Pa is measured as 14 nm, smaller than the thickness of deposited Cr film. Figures 3(c)-(e) show the cross-section SEM images of the n-LIPSSs formed at air pressures $P = 4.2 \times 10^2$ Pa, 1.1 Pa and 2.2×10^{-5} Pa, respectively. Different from the a-LIPSSs, the n-LIPSSs present a strong material removal process, resulting in a deep penetrating ablation into the Si substrate. The average modulated depth of n-LIPSSs decreases from 253.7 nm to 214 nm with the reduction of air pressure from $P = 4.2 \times 10^2$ Pa to 2.2×10^{-5} Pa. The corresponding variations for both the structure depth and the height at different air pressures are illustrated in Fig. 3(f).

As the air pressure is decreased from $P = 4.2 \times 10^2$ Pa to 2.2×10^{-5} Pa, the film material covered on the Si substrate tends to become thinner [Figs. 3(c)-(e)]. Specifically, at the condition of $P = 4.2 \times 10^2$ Pa, the n-LIPSSs seem to be buried by a snow-like covering with a thickness of 71 ± 6 nm. Whereas at $P = 2.2 \times 10^{-5}$ Pa, the obtained structures reveal the clear narrow-necked profiles with a 50 nm-thick covering as thick as the initially evaporated Cr film. According to the previous report, the redeposition of nanoparticles from the ablation plume can be effectively prohibited when the surrounding air pressure is lower than $P = 1.0 \times 10^3$ Pa [25]. Thus, the thickness variation of the covering material in our experiments should be ascribed to other factors. To identify the reasons, we analyzed the material compositions in the laser structured areas using a micro-Raman spectroscopy (Horiba Jobin Yvon) with an excitation wavelength at 532 nm. The measured results demonstrate the presence of two Raman peaks at 553 cm^{-1} and 665 cm^{-1} related to the Cr_2O_3 and the CrO_2 [26], respectively. Their Raman signal intensities become stronger with the increase of air pressure, as shown in Fig. 3(g). Therefore, it is clear that the thickness variation of the covering material on the Si substrate is originated from the volume expansion of Cr film after oxidation.

To understand the transition mechanisms, we investigate the structural evolution with the applied pulse number N for a given laser energy $E_0 = 4.21$ μJ at different air pressures. Wherein, an electromechanical shutter is utilized to provide the desired pulse number impinging on the same spot area on the sample surface. For the sake of comparison, Figs. 4(a)-(b) respectively show the typical optical micrographs of the target surface irradiated by different pulse numbers at $P = 1.0 \times 10^5$ Pa and 2.2×10^{-5} Pa, which correspond to the formation of a-LIPSSs and n-LIPSSs, respectively. In addition, the elliptical laser modification shown in the optical micrographs stems from the formation of astigmatism in the laser processing system due to the slightly slanted placement of the vacuum window to the vertical plane. From these pictures, we can find that
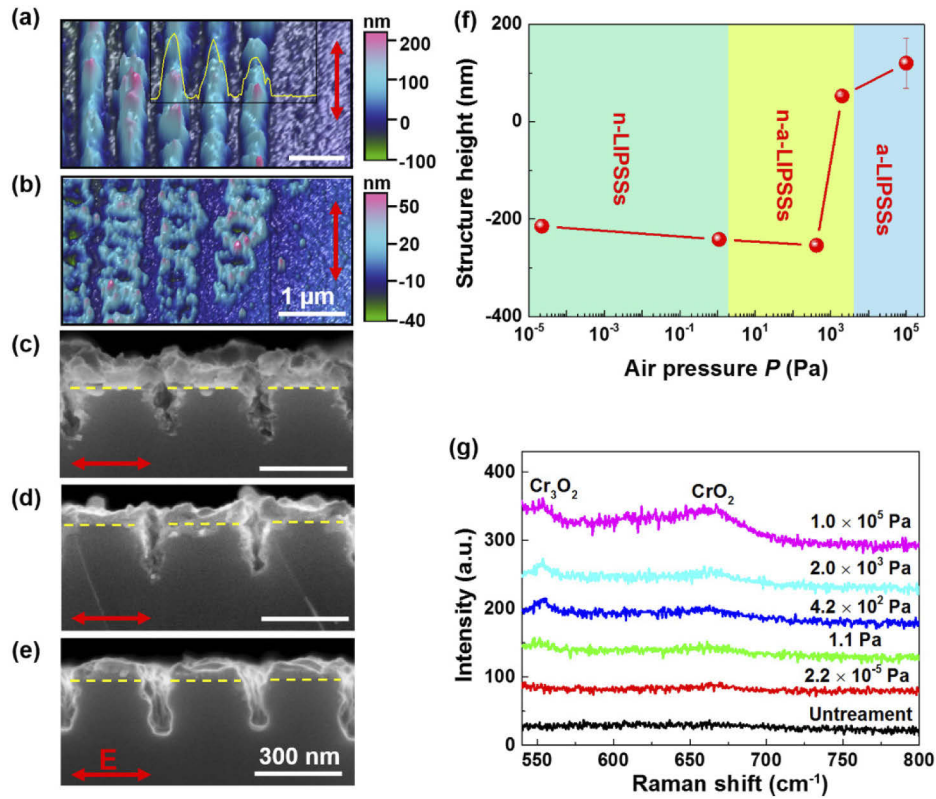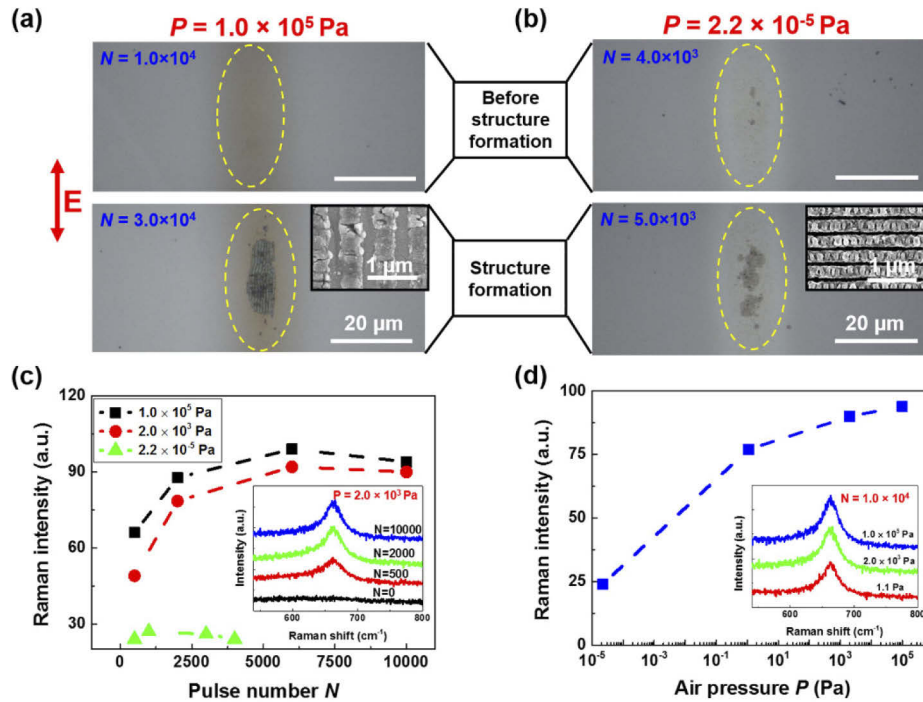
Fig. 3. AFM images of laser-induced structures produced at (a) atmospheric pressure and (b) $P = 2.0 \times 10^3$ Pa. The inset in panel (a) illustrates the cross-sectional profile of the a-LIPSSs. Side-view SEM images for n-LIPSSs produced at different reduced air pressures (c) $P = 4.2 \times 10^2$ Pa, (d) $P = 1.1$ Pa and (e) $P = 2.2 \times 10^{-5}$ Pa. (f) Measured modulation height for the laser-induced structures at different air pressures. (g) Measured Raman spectra in the structure areas produced by femtosecond laser pulses at different air pressures. The scale bar in panels (a)-(b) is consistent, and the same situation for panels (c)-(d). The yellow dotted lines in panels (c)-(e) indicate the boundary between the film material and Si substrate.

the a-LIPSSs cannot be generated until the applied pulse number is larger than $N = 3.0 \times 10^4$ in atmospheric pressure; however, the formation of n-LIPSSs only requires the pulse number larger than $N = 5.0 \times 10^3$ at $P = 2.2 \times 10^{-5}$ Pa. These results indicate that the pulse number requirement for the formation of a-LIPSSs is an almost five-fold increase compared with the n-LIPSSs. In addition, it can be also found that the optical color in the laser-irradiated areas before the structure formation turns to be slightly different for these two cases, which may be ascribed to the change of material properties due to the laser-induced oxidation.

In order to clarify this point, we performed Raman analyses in the laser-irradiated areas without the structure formation at different air pressures. In comparison of the Raman spectra in the structure areas [Fig. 3(g)], only the characteristic peak of CrO_2 at 665 cm^{-1} is detected within a spectrum range of 540-800 cm^{-1}. The absence of Cr_2O_3 should be ascribed to the exposure of few pulse numbers [26]. This phenomenon can be also exemplified by the Raman spectra obtained at $P = 2.0 \times 10^3$ Pa, as shown in the inset of Fig. 4(c). In addition, we also find that the measured Raman intensity of CrO_2 closely depends on both the air pressure and the applied pulse number. For example, in the cases of high air pressure ($P = 2.0 \times 10^3$ Pa and 1.0×10^5 Pa), the measured Raman intensity of CrO_2 increases dramatically and finally reaches a saturated level

Fig. 4. Optical micrographs of the 50-nm thick Cr/Si film irradiated by a sequence of laser pulses at different air pressures: (a) $P = 1.0 \times 10^5$ Pa; (b) $P = 2.2 \times 10^{-5}$ Pa. The insets show the magnified SEM images of laser-induced structures. Here, the yellow-dotted ellipses indicate the laser-irradiated areas. (c) and (d) respectively show the measured Raman intensity of CrO_2 as a function of the applied pulse number and air pressure in the laser-irradiated areas prior to the structure formation. In panels (c) and (d), the insets show the measured Raman spectra at the given air pressure $P = 2.0 \times 10^3$ Pa and the pulse number $N = 1.0 \times 10^4$, respectively.

with the continuous increase of the pulse number. While for the high vacuum condition ($P = 2.2 \times 10^{-5}$ Pa), the laser-induced oxidation is effectively prohibited due to lacking available oxygen. Moreover, the measured Raman intensity of CrO_2 versus the air pressure is also illustrated in Fig. 4(d), where the applied pulse numbers reach the maximum prior to structure formation for each case in our experiments. It can be found that the variation of Raman intensity of CrO_2 is almost proportional to the air pressure, which can be also visualized by the variation of the peak intensity at 665 cm^{-1} measured at different air pressures, as shown in the inset of Fig. 4(d). Therefore, a superficial oxidation layer can be considered to be induced on the Cr film surface by the preceding laser pulses before the structure formation. Besides, the amount of laser-induced oxide presents a linear dependence on the air pressure, which may affect the formation of LIPSSs.

Although the underlying mechanism for LIPSSs is still controversial, a theory of interference between the incident laser light and the excited surface electromagnetic waves is widely accepted. In the ambient air environment, the subwavelength a-LIPSSs are found to be formed on the Cr/Si films after femtosecond laser irradiation in our experiments. Using the Sipe theory with a small filling factor, Dostovalov *et al.* emphasized that the formation of a-LIPSSs should be ascribed to the generation of transverse-electric scattered surface wave (TE-SSW) due to the dipole-like scattering of surface roughness on the purely metallic surface [23]. However, Florian et al. recently have demonstrated that the superficial oxide layer is required for the formation of subwavelength a-LIPSSs on the chromium nitride (CrN) surface using the FDTD simulation

[27]. This prediction can be supported by our experiment results, where the oxide layer is experimentally evidenced in the laser-irradiated areas prior to the a-LIPSSs formation at high air pressure conditions. Besides, for the lower air pressure conditions, the amount of oxide is reduced, which consequently leads to the disappearance of a-LIPSSs. Therefore, a physical scenario is supposed that the TE-SSW is first excited on the oxide layer due to the scattering of surface roughness to the subsequent laser pulses, and then the resultant periodic intensity fringes from interference between the incident light and the TE-SSW evolve into the bulge-like a-LIPSSs with the strong material oxidation at the intensity maxima, as shown in Fig. 5(a).
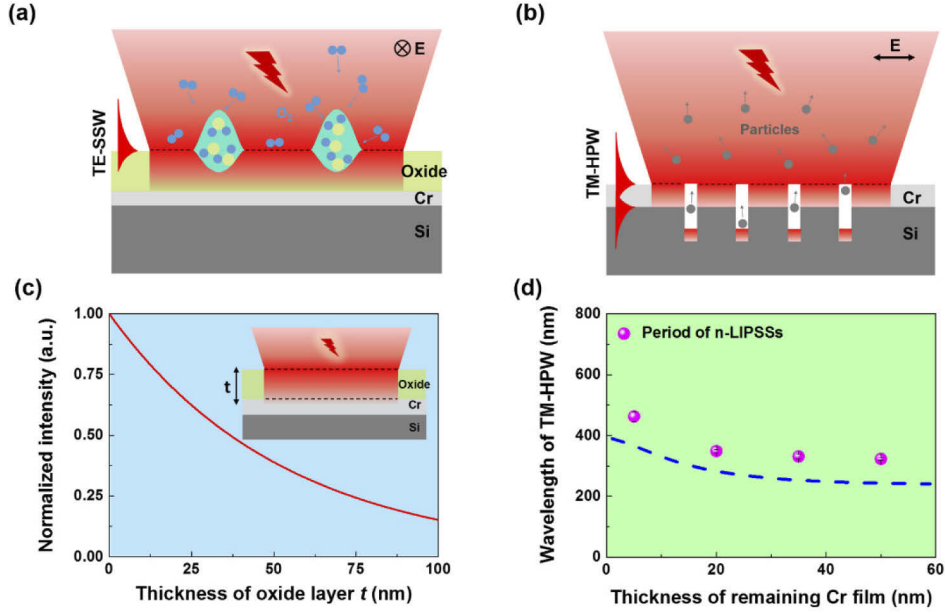
Fig. 5. Schematic diagrams for the formation of two types of LIPSSs: (a) a-LIPSSs at atmospheric environment; (b) n-LIPSSs at high vacuum conditions. Here, E represents the direction of laser polarization. (c) Normalized transmission for the laser-induced oxide layer as a function of its thickness. (d) The dependence of wavelength for the TM-HPW on the thickness of the remaining Cr film. The solid circles represent the measured periods of n-LIPSSs at different air pressures.

However, in the high vacuum circumstance ($P = 2.2 \times 10^{-5}$ Pa), the oxidation of Cr film can be effectively suppressed due to lacking available oxygen, which indicates the direct interaction between the femtosecond laser pulses and the thin Cr film. In this case, a transverse-magnetic hybrid plasmon wave (TM-HPW) can be generated within the thin Cr film due to the coupling of two transverse-magnetic surface plasmon waves at the interfaces of vacuum/Cr and Cr/Si [28,29], and then results in the formation of deep-subwavelength n-LIPSSs, as shown in Fig. 5(b). For a thin metallic film ε_2 with a thickness h surrounded by the dielectric media ε_1 and ε_3, the dispersion relation of TM-HPW can be expressed as follows:

$$\left(\varepsilon_1\varepsilon_3 S_2^2 + \varepsilon_2^2 S_1 S_3\right)\tanh\left(S_2 h\right) + \left[S_2\left(\varepsilon_1 S_3 + \varepsilon_3 S_1\right)\varepsilon_2\right] = 0, \tag{1}$$

$$S_j^2 = \beta^2 - \varepsilon_j k_0^2,$$

where $j = 1$, 2 or 3 is related to vacuum, Cr film and Si substrate, respectively; β and k_0 are the propagation constants for the TM-HPW and the laser light, respectively. The wavelength of TM-HPW can be given by $\lambda = 2\pi/\mathrm{Re}\,(\beta)$.

In addition, with the decline of air pressure from the atmospheric environment ($P = 1.0 \times 10^5$ Pa) to the high vacuum ($P = 1.0 \times 10^{-5}$ Pa), the laser-induced structures undergo a transition from the a-LIPSSs to n-LIPSSs accompanied with the reducing oxidization process. It should be noted that apart from the TE-SSW excitation, the preformed oxide layer can also attenuate the subsequent laser energy onto the thin Cr film, as shown in Fig. 5(c), where the skin depth of the oxide layer is accounted as $\delta = 106$ nm at 800 nm laser wavelength with the permittivity $\varepsilon_o = 3.21 + i5.15$ [30]. Therefore, a competitive excitation between TE-SSW and TM-HPW is established and consequently triggers the transition of LIPSSs. More specifically, at the atmospheric pressure, a quite thick oxide layer is induced in the laser-irradiated areas due to the strong oxidation, which seriously prevents the excitation of TM-HPW by absorbing most of the incident laser energy. As a result, the individual excitation of TE-SSW on the top surface of the film leads to the only formation of subwavelength a-LIPSSs. While with the reduction of air pressure, the thickness of the preformed oxide layer becomes thinner, which allows more laser energy to reach the remaining Cr film underneath the oxide layer. In this case, both TE-SSW and TM-HPW can be excited simultaneously, eventually resulting in the coexistence of a-LIPSSs and n-LIPSSs. Besides, the formation of nanoholes on the ridges of a-LIPSSs can be understood by the material ablation from the enhanced intensity on the overlapping areas of these two surface waves. However, as for the high vacuum conditions, the oxidation process is greatly diminished, so that the individual excitation of TM-HPW leads to the only formation of deep-subwavelength n-LIPSSs. Furthermore, the wavelength of TM-HPW generated within the oxide/Cr/Si system is calculated, where the thickness of Cr film is reduced due to the increased oxidation. The calculated wavelengths match well with the measured periods of n-LIPSSs at different air pressures, as shown in Fig. 5(d).

4. Conclusions

In summary, we have investigated an intriguing transition of LIPSSs on 50-nm thick Cr/Si films irradiated by 800 nm femtosecond laser within different air pressure environments. Under the atmospheric pressure ($P = 1.0 \times 10^5$ Pa), the laser-irradiated surface was found to be decorated with the subwavelength a-LIPSSs with the metal-oxide bulge morphology. In the high vacuum condition ($P = 1.0 \times 10^{-5}$ Pa), however, the laser-irradiated surface was seen to be developed with the deep-subwavelength n-LIPSSs with the pronounced ablation morphology. When the air pressure was adjusted to a moderate range, the aforementioned two types of structures were found to coexist on the film surface.

To discover the physical origins of the structure transition, a micro-Raman spectroscopy was employed to analyze the chemical composition in the laser-irradiated areas before the formation of different structures. It was found that the amount of metal oxide (CrO_2) tended to increase with the higher values of both the applied pulse number and air pressure. In other words, the formation of the metal oxide layer induced by the proceeding laser pulses plays a switching role in the structure development. As a result, two different surface waves, TE-SSW and TM-HPW, can be selectively excited according to the oxidation degree, which consequently determines the category of LIPSSs. Moreover, the calculated wavelengths of TM-HPW versus the thickness of the remaining Cr film presented a good agreement with the measured periods of n-LIPSSs at different air pressures.

In comparison to Ref. 23, it is found here that the a-LIPSSs are likely to generate in the strong oxidation situation; however, the n-LIPSSs are preferable to form in the weak or non-oxidation situation. The observation discrepancy may be due to the influence of the substrate that will be comprehensively investigated in our future research. Besides, the structure transition is ascribed to the thickness variation of the preformed oxide layer which determines the excitation of TE-SSW and TM-HPW. In brief, the oxidation ruled category transition further sheds light

on the importance of the oxide layer on the formation of LIPSSs and also provides a feasible approach in their controllable fabrication.

References

1. A. Borowiec and H. K. Haugen, "Subwavelength ripple formation on the surfaces of compound semiconductors irradiated with femtosecond laser pulses," Appl. Phys. Lett. **82**(25), 4462–4464 (2003).
2. J. Bonse, A. Rosenfeld, and J. Krüger, "On the role of surface plasmon polaritons in the formation of laser-induced periodic surface structures upon irradiation of silicon by femtosecond-laser pulses," J. Appl. Phys. **106**(10), 104910 (2009).
3. G. D. Tsibidis, M. Barberoglou, P. A. Loukakos, E. Stratakis, and C. Fotakis, "Dynamics of ripple formation on silicon surfaces by ultrashort laser pulses in subablation conditions," Phys. Rev. B **86**(11), 115316 (2012).
4. L. Wang, Q.-D. Chen, X.-W. Cao, R. Buividas, X. Wang, S. Juodkazis, and H.-B. Sun, "Plasmonic nano-printing: large-area nanoscale energy deposition for efficient surface texturing," Light: Sci. Appl. **6**(12), e17112 (2017).
5. J. Bonse, R. Koter, M. Hartelt, D. Spaltmann, S. Pentzien, S. Höhm, A. Rosenfeld, and J. Krüger, "Femtosecond laser-induced periodic surface structures on steel and titanium alloy for tribological applications," Appl. Phys. A **117**(1), 103–110 (2014).
6. B. Dusser, Z. Sagan, H. Soder, N. Faure, J. P. Colombier, M. Jourlin, and E. Audouard, "Controlled nanostructrures formation by ultra fast laser pulses for color marking," Opt. Express **18**(3), 2913–2924 (2010).
7. T. Shinonaga, M. Tsukamoto, T. Kawa, P. Chen, A. Nagai, and T. Hanawa, "Formation of periodic nanostructures using a femtosecond laser to control cell spreading on titanium," Appl. Phys. B **119**(3), 493–496 (2015).
8. J. P. Colombier, F. Garrelie, N. Faure, S. Reynaud, M. Bounhalli, E. Audouard, R. Stoian, and F. Pigeon, "Effects of electron-phonon coupling and electron diffusion on ripples growth on ultrafast-laser-irradiated metals," J. Appl. Phys. **111**(2), 024902 (2012).
9. I. Gnilitskyi, T. J. Derrien, Y. Levy, N. M. Bulgakova, T. Mocek, and L. Orazi, "High-speed manufacturing of highly regular femtosecond laser-induced periodic surface structures: physical origin of regularity," Sci. Rep. **7**(1), 8485 (2017).
10. S. Hou, Y. Huo, P. Xiong, Y. Zhang, S. Zhang, T. Jia, Z. Sun, J. Qiu, and Z. Xu, "Formation of long- and short-periodic nanoripples on stainless steel irradiated by femtosecond laser pulses," J. Phys. D: Appl. Phys. **44**(50), 505401 (2011).
11. F. Wang, B. Zhao, Y. Lei, J. Yang, and C. Guo, "Producing anomalous uniform periodic nanostructures on Cr thin films by femtosecond laser irradiation in vacuum," Opt. Lett. **45**(6), 1301–1304 (2020).
12. J. Wang and C. Guo, "Ultrafast dynamics of femtosecond laser-induced periodic surface pattern formation on metals," Appl. Phys. Lett. **87**(25), 251914 (2005).
13. Y. Yang, J. Yang, C. Liang, H. Wang, X. Zhu, D. Kuang, and Y. Yang, "Sub-wavelength surface structuring of NiTi alloy by femtosecond laser pulses," Appl. Phys. A **92**(3), 635–642 (2008).
14. J. Bonse, S. Höhm, A. Rosenfeld, and J. Krüger, "Sub-100-nm laser-induced periodic surface structures upon irradiation of titanium by Ti:sapphire femtosecond laser pulses in air," Appl. Phys. A **110**(3), 547–551 (2013).
15. A. V. Dostovalov, V. P. Korolkov, K. A. Okotrub, K. A. Bronnikov, and S. A. Babin, "Oxide composition and period variation of thermochemical LIPSS on chromium films with different thickness," Opt. Express **26**(6), 7712–7723 (2018).
16. X. F. Li, C. Y. Zhang, H. Li, Q. F. Dai, S. Lan, and S. L. Tie, "Formation of 100-nm periodic structures on a titanium surface by exploiting the oxidation and third harmonic generation induced by femtosecond laser pulses," Opt. Express **22**(23), 28086–28099 (2014).
17. C. S. Nathala, A. Ajami, A. A. Ionin, S. I. Kudryashov, S. V. Makarov, T. Ganz, A. Assion, and W. Husinsky, "Experimental study of fs-laser induced sub-100-nm periodic surface structures on titanium," Opt. Express **23**(5), 5915–5929 (2015).
18. B. Öktem, I. Pavlov, S. Ilday, H. Kalaycıoğlu, A. Rybak, S. Yavaş, M. Erdoğan, and FÖ Ilday, "Nonlinear laser lithography for indefinitely large-area nanostructuring with femtosecond pulses," Nat. Photonics **7**(11), 897–901 (2013).
19. M. Huang, F. Zhao, Y. Cheng, N. Xu, and Z. Xu, "Origin of Laser-Induced Near-Subwavelength Ripples: Interference between Surface Plasmons and Incident Laser," ACS Nano **3**(12), 4062–4070 (2009).
20. S. Sakabe, M. Hashida, S. Tokita, S. Namba, and K. Okamuro, "Mechanism for self-formation of periodic grating structures on a metal surface by a femtosecond laser pulse," Phys. Rev. B **79**(3), 033409 (2009).
21. J. E. Sipe, J. F. Young, J. S. Preston, and H. M. Vandriel, "Laser-induced periodic surface structure. I. Theory," Phys. Rev. B **27**(2), 1141–1154 (1983).

22. S. I. Kudryashov, S. V. Makarov, A. A. Ionin, C. S. Nathala, A. Ajami, T. Ganz, A. Assion, and W. Husinsky, "Dynamic polarization flip in nanoripples on photoexcited Ti surface near its surface plasmon resonance," Opt. Lett. **40**(21), 4967–4970 (2015).

23. A. V. Dostovalov, T. J. Y. Derrien, S. A. Lizunov, F. Přeučil, K. A. Okotrub, T. Mocek, V. P. Korolkov, S. A. Babin, and N. M. Bulgakova, "LIPSS on thin metallic films: New insights from multiplicity of laser-excited electromagnetic modes and efficiency of metal oxidation," Appl. Surf. Sci. **491**, 650–658 (2019).

24. A. Rudenko, A. Abou-Saleh, F. Pigeon, C. Mauclair, F. Garrelie, R. Stoian, and J. P. Colombier, "High-frequency periodic patterns driven by non-radiative fields coupled with Marangoni convection instabilities on laser-excited metal surfaces," Acta Mater. **194**, 93–105 (2020).

25. J. Jj Nivas, F. Gesuele, E. Allahyari, S. L. Oscurato, R. Fittipaldi, A. Vecchione, R. Bruzzese, and S. Amoruso, "Effects of ambient air pressure on surface structures produced by ultrashort laser pulse irradiation," Opt. Lett. **42**(14), 2710–2713 (2017).

26. A. V. Baranov, K. V. Bogdanov, A. V. Fedorov, M. V. Yarchuk, A. I. Ivanov, V. P. Veiko, and K. Berwick, "Micro-Raman characterization of laser-induced local thermo-oxidation of thin chromium films," J. Raman Spectrosc. **42**(9), 1780–1783 (2011).

27. C. Florian, J. L. Deziel, S. V. Kirner, J. Siegel, and J. Bonse, "The Role of the Laser-Induced Oxide Layer in the Formation of Laser-Induced Periodic Surface Structures," Nanomaterials **10**(1), 147 (2020).

28. J. J. Burke, G. I. Stegeman, and T. Tamir, "Surface-polariton-like waves guided by thin, lossy metal films," Phys. Rev. B **33**(8), 5186–5201 (1986).

29. J. R. S. Fuzi Yang and G. W. Bradberry, "Long-range surface modes supported by thin films," Phys. Rev. B **44**(11), 5855–5872 (1991).

30. L. L. Chase, "Optical properties of CrO_2 and MoO_2 from 0.1 to 6 eV," Phys. Rev. B **10**(6), 2226–2231 (1974).